High Speed Imager AXAF Calibration Microchannel Plate Detector

I. N. Evans, E. M. Kellogg, W. C. McDermott, M. P. Ordway, J. M. Rosenberg,
and B. J. Wargelin

Smithsonian Astrophysical Observatory, 60 Garden Street, Cambridge MA   02138   USA

ABSTRACT

The design and implementation of the High Speed Imager (HSI) microchannel plate based imaging x-ray detector used for the calibration of the Advanced X-ray Astrophysics Facility (AXAF) High Resolution Mirror Assembly (HRMA) and Objective Transmission Gratings (OTGs) is described. The similarities between the HSI and the AXAF High Resolution Camera (HRC) are discussed, as well as the modifications to the original HRC-like design needed to operate the detector at count rates up to $\sim 2000\,\mathrm{Hz}$ used during the HRMA calibration.

The imaging performance of the detector that is necessary to achieve the calibration error budget for the HRMA is discussed. Details of the actual performance of the HSI are provided in terms of key parameters such as spatial uniformity and linearity, imaging resolution, and counting rate limitations. The measurement techniques used to verify and calibrate the requisite detector performance are described.

Keywords: AXAF calibration, microchannel plate, x-ray instrumentation

1. INTRODUCTION

The High Speed Imager is a microchannel plate (MCP) based x-ray imaging detector that forms part of the HRMA x-ray detector system (HXDS) used during phase 1 of the AXAF calibration. Developed by the Smithsonian Astrophysical Observatory, the HXDS comprises a set of beam intensity normalization detectors together with a detector assembly designed to be placed at the focal surface of the HRMA. The detector assembly mounts a pair of flow proportional counters, a high purity Ge solid-state detector, ancilliary support hardware (such as a series of apertures), and the HSI detector, mounted on a set of precision translation stages. This configuration provides the flexibility necessary to obtain the calibration data required to characterize the performance of the HRMA and OTGs prior to flight.

Since the HSI is used solely to support the calibration of AXAF, the design is optimized for this purpose. Two primary design requirements are that the imager (a) have excellent spatial resolution, implying a small pixel size and good imaging fidelity, and (b) be capable of responding linearly over a broad range of input flux, implying that the detector have a wide dynamic range and a high maximum count rate without significant dead-time corrections. The ability to support high count rates is particularly important for a detector that is used for AXAF calibrations where high flux intensities are expected in the focused beam from the HRMA. A maximum count rate goal of 2000 Hz is incorporated into the imager design.

In this paper the current status of the HSI is described. First, a description of the hardware configuration is provided, including detailed information about critical design parameters. Next, the current calibration state of the detector is described, using sample calibration data where possible. Finally, some examples of data obtained using the HSI during phase 1 of the AXAF calibration are presented.

2. HARDWARE DESCRIPTION

The imager consists of a detector head assembly (Fig. 1) and a post-processing electronics rack. The detector head assembly incorporates the x-ray sensitive MCP stack and associated hardware (ion shield and permanent mask assembly), together with the cross-grid charge detector (CGCD) assembly that reads out the electron charge cloud formed by the MCP stack in response to an x-ray event, and a set of preamplifiers that amplify and shape the signal voltages read out from the CGCD taps. The post-processing electronics rack includes event detection, coarse position determination, and veto logic, and converts the analog outputs from the preamplifiers into a digital telemetry stream that can be read by computer. A block diagram of the imager is presented in Figure 2.
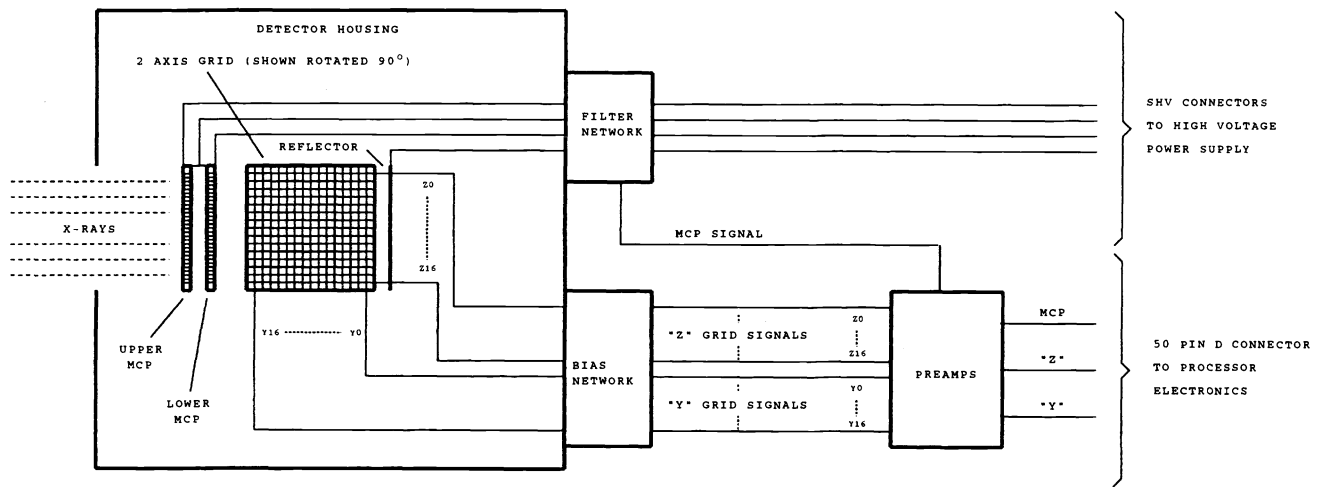
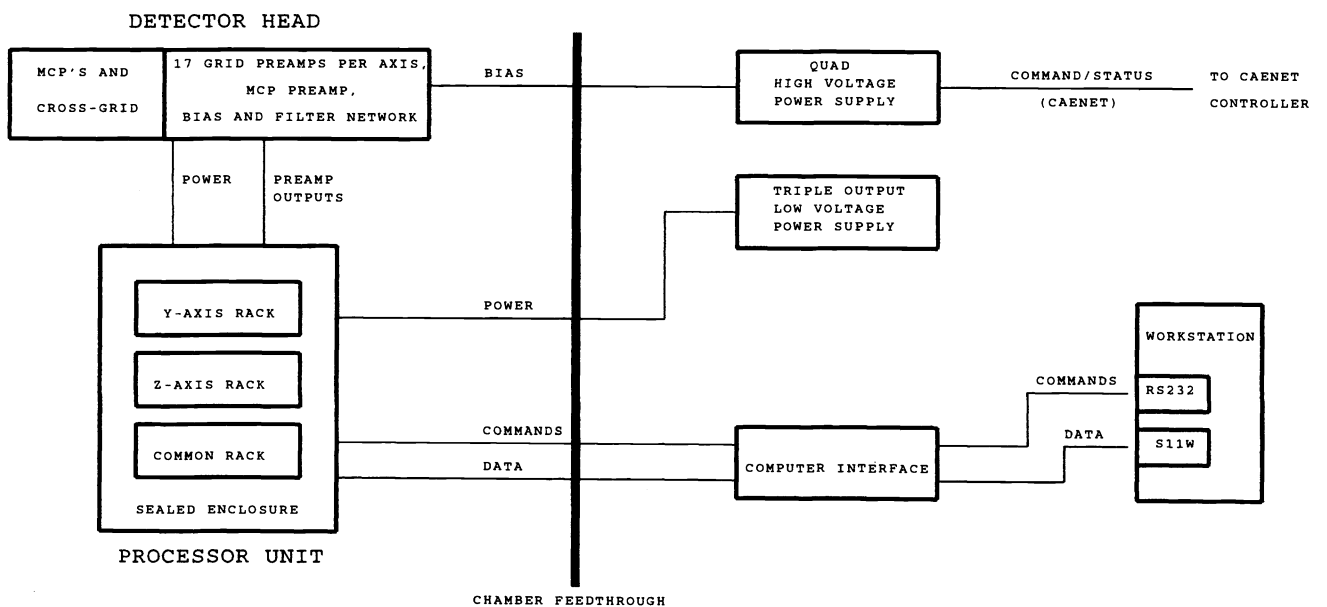**Figure 1.** High Speed Imager detector head block diagram. The ion shield is not shown in this figure.

Figure 2. High Speed Imager block diagram.

19

2.1. Microchannel plate assembly

The active elements of the imager are a matched pair of MCPs mounted in a chevron configuration, providing a total electron gain of $\sim 1 \times 10^7$ under normal operating conditions.

Each MCP is cylindrical in shape with an outside diameter of 24.8 ± 0.1 mm and a thickness of 0.64 ± 0.04 mm. The individual channels are nominally $8 \pm 1\,\mu$m diameter (yielding an $80 : 1$ L/D ratio) arranged in a hexagonal close-packed structure with $10 \pm 1\,\mu$m (typically $9.5\,\mu$m) channel-to-channel spacing. Input and output electrodes are formed by evaporating Nichrome 80/20 onto the front and back surfaces of each MCP over an active area no smaller than 18 mm diameter. The channels are end-spoiled by extending the input and output electrodes into the channels by 0.5 ± 0.2 channel diameters.

To produce the chevron configuration, for each MCP the channel centerlines are biased by $6^\circ \pm 1^\circ$ relative to the normal to the MCP input surface. The bias angle is marked by a visible fiducial on the input surface of each MCP. During mounting, the MCPs are clocked so that the bias angle fiducial mark is aligned with the imager $+Y$ for the front MCP and $-Y$ for the back MCP, with an accuracy of $\sim 20'$. The output surface of the front MCP and the input surface of the back MCP are spaced $\sim 51\,\mu$m apart by an electrode that provides a single high voltage potential to both of these surfaces.

The MCPs are manufactured by Galileo Electro-Optics Corporation (GEOC) using GEOC MCP 10 "long-life" glass microchannel plate glass. This glass formulation is chosen because the charge extraction lifetime reported by the manufacturer (at least $30\,\mathrm{C\,cm^{-2}}$) is an order of magnitude longer than most other MCP glass formulations. Over the duration of the complete AXAF HRMA calibration program, charge extraction effects can be important in localized areas of the imager for glass formulations with significantly lower charge extraction lifetimes than that used. Prior to delivery, the MCPs are baked and UV scrubbed by the vendor to an extracted charge level of $\sim 0.25\,\mathrm{C\,cm^{-2}}$.

During much of the imager development and initial characterization, a CsI coating was included on the input surface of the front MCP as a photocathode. Bialkali photocathodes are known to increase significantly the detector quantum efficiency at energies between ~ 100 eV and ~ 500 eV as well as at AXAF energies $\gtrsim 1.5$ keV,[1] and similar photocathodes are used in the HRC.[2] Unfortunately, a hardware failure that occured shortly before the AXAF HRMA calibration required the MCPs to be replaced with a stack that did not incorporate a photocathode.

Located approximately 12.7 mm ahead of the input surface of the front MCP is an ion shield consisting of a thin film composite of ~ 250 Å of Al deposited on a ~ 1000 Å Lexan base. The ion shield used in the HSI is significantly thinner than that developed for the HRC. For the latter, excellent UV absorption is a strong requirement because the flight detector must block geo-coronal Lyα from entering the MCPs. The absence of UV light in the enclosed X-Ray Calibration Facility (XRCF) test chamber, and the need to maximize quantum efficiency for calibration at low x-ray energies, mandates the use of thinner shield material for the HSI.

The ion shield was added to the imager late in the development cycle after preliminary tests with an MCP stack coated with a CsI photocathode revealed the presence of localized structures in the detector background. Broad regions of enhanced emission several mm across, together with sharp, well-defined approximately linear "streaks" ranging up to of order 0.5 mm wide and a few mm long were observed. Localized background intensities were sometimes as much as $20\times$ the uniform background rate. The position, intensity, and morphology of the background structure varied both with applied voltage and with time, with significant changes on a timescale of one day.

The uneven background is at least partly due to non-uniformities in the electric field near the photocathode producing localized enhancements caused by thermal electrons emitted from the interchannel regions striking the MCP with a rate proportional to the localized field strength. This problem is solved by generating artificially a weak but uniform electric field immediately in front of the photocathode that will attract these electrons away from striking the photocathode.[3] The ion shield used in the HSI was biased by $+200$ V relative to the input surface of the front MCP.

As described previously, the CsI coated MCPs were replaced with uncoated MCPs prior to AXAF calibration. Previous data obtained using uncoated MCPs demonstrate that the localized background features observed with the CsI coated MCPs are not present, apparently eliminating the requirement for the ion shield. However, to minimize hardware configuration changes the ion shield was retained.

Between the ion shield and the front MCP is a "permanent" mask assembly. The permanent mask is mounted ~ 0.2 mm from the input surface of the front MCP and provides a variety of occulting features designed to block

portions of the x-ray beam from the HRMA or HRMA/OTG. A pair of "cusps" with 60° blocking angles are provided to obscure the center of the HRMA point response function (PRF) to permit measurements of the PRF outer core ($r \gtrsim 1''$) to be obtained with reasonable count rates while blocking the extremely bright inner core of the flux profile. The edges of the permanent mask are aligned approximately parallel to and perpendicular to the grating dispersion directions to allow the detection of faint features near to bright grating orders. The layout of the permanent mask provides an unambiguous orientation reference for the imager.

2.2. Cross-grid charge detector assembly

The charge cloud generated by electron amplification in the MCP stack of an incident x-ray event is read out using the CGCD assembly. The design of the CGCD used in the HSI is similar to that employed in the *Einstein* HRI.[4]

In each of the orthogonal imager Y, Z axes, the collected charge is read out by using a grid of uniformly spaced wires that are positioned behind the output surface of the back MCP. The wires are $\sim 102\,\mu$m diameter spaced on $\sim 206\,\mu$m centers. A total of 129 wires in each axis yields a total dimension $\sim 26.3 \times 26.3$ mm, large enough to span the area covered by the MCPs. Adjacent wires in each axis are connected electrically through $40\,\text{k}\Omega$ resistors, and taps on every eighth wire provide electrical connections to a set of 17 preamplifiers that collect the charge deposited on the cross-grid.

The spacing between the Y and Z grids is $\sim 206\,\mu$m center-to-center, with the Z grid positioned in front of the Y grid, ~ 0.84 mm behind the output surface of the back MCP. In the HSI the output surface of back MCP is biased by -300 V with respect to the cross-grid. Since the Z grid partly obscures the Y grid from the charge cloud produced by electron amplification in the MCPs, the Y and Z cross-grids must be biased differently in order to ensure that each grid collects approximately the same amount of charge. The bias voltage is fed into the individual grids through the first, middle, and last taps on each axis. As part of the initial setup procedure, the relative bias is adjusted so that the summed charge collected from the preamplifiers on each axis is the same.

The material used for the cross-grid wires is manufactured by the J. M. Ney company, and comprises an alloy principally of Au, Cu, and Pt plus some other metals, designated NEYORO-G.

Located ~ 0.38 mm behind the back cross-grid wires is a reflector plane electrode consisting of a Au over Nichrome surface coat on an alumina substrate. The reflector is biased by -150 V with respect to the cross-grid, effectively reflecting any electrons from the charge cloud that may pass through the cross-grid wires back to the cross-grid so that the total charge can be measured accurately.

2.3. Post-processing electronics

The analog signals from the cross-grid preamplifiers are processed by the HSI post-processing electronics assembly. This unit is responsible for combining the analog signals to detect individual x-ray events, determine the (Y, Z) position on the cross-grid of any events detected, accept or reject events based on a set of (programmable) criteria, and transmit a telemetry stream describing the accepted events via computer interface to be recorded by software. The post-processing electronics is based primarily on the HRC laboratory brass-board design, with modifications principally to allow operation at an event rate $10\times$ higher than the maximum event rate for the flight detector.

An x-ray event incident on the detector causes electron multiplication in the MCP stack. The resulting charge cloud generates a voltage in each tap of the CGCD that is amplified and buffered by the detector unit preamplifiers. When the summed analog output from the 17 Y and 17 Z preamplifiers exceeds a programmable "trigger level" threshold, an event is detected by the post-processing electronics. The summed analog level is digitized to produce a pulse height that will be recorded if the event is not rejected by the processing electronics.

The coarse position of the peak of the charge cloud in each axis is approximated by identifying the lowest and highest taps that have a signal level greater than a predetermined threshold. The signal levels from the two preamplifiers that are closest to the mid-position between the lowest and highest taps that exceed the threshold are compared, and the tap with the highest signal level is considered the center tap for the coarse position determination. The signal levels from this tap and the two adjacent taps are digitized and will be used for fine position determination.

Once the coarse position is determined, the event is subject to a variety of tests by the programmable veto logic to assure its validity. The principal validity tests are (a) the event is detected in both the Y and Z axes, (b) the event's pulse height is greater than a programmable lower level discriminator setting and less than a programmable upper

21

level discriminator setting, and (c) enough time since the previous event has elapsed so that the signal sample and hold electronics and the event processing electronics have recovered and completed processing the previous event. If the event fails the validity checks then it is nevertheless counted by the electronics, but the position and pulse height of the event are not recorded.

Assuming that the event passes all the validity checks, then the signal outputs from the 3 preamplifiers in each axis that are selected by the coarse position logic are digitized and output, together with the pulse height and timing information, to the telemetry stream.

The fine position of an event is computed from the telemetry stream using a simple three point centroid algorithm for each axis. If A, B, and C are the digitized outputs of the preamplifiers corresponding to taps $n - 1$, n, and $n + 1$ respectively, where tap n corresponds to the event position determined by the coarse event position logic, then the fine position relative to tap n is given by $F = (C - A)/B \times 256$, where the spacing between consecutive taps is defined to be equal to 256 pixels (corresponding to a pixel size of $\sim 6.43\,\mu m$). Note that for a perfect detector with no noise and a symmetric charge distribution, $-128 \leq F \leq 128$, since otherwise the coarse position logic would have selected one of the adjacent taps as the coarse position. In practice, electronic noise or charge cloud asymmetry can sometimes result in a value for F that is outside these bounds.

The three tap algorithm has a built-in bias that distorts the fine position for events that are not centered on a tap. Consider an event centered approximately halfway between taps n and $n + 1$. In this case, the signals from taps n and $n + 1$ will be approximately equal, and the signals from taps $n - 1$ and $n + 2$ will be approximately equal, but with lower intensity. If tap n is selected as the coarse position, then the three tap centroid will not include the signal from tap $n + 2$ in the centroid computation, and will therefore bias the fine position in the direction of tap n. Conversely, if tap $n + 1$ is selected as the coarse position, then the three tap centroid will not include the signal from tap $n - 1$ in the centroid computation, and will therefore bias the fine position in the direction of tap $n + 1$. This position bias creates an artificial "gap" near the positions halfway between two taps that must be corrected for by software post-processing.

To assist checkout of the detector electronics the HSI is equipped with a self-test mode. In this mode a test pulse is coupled capacitively into the back MCP, resulting in an approximately uniform charge being injected into all of the Y and Z axis cross-grid taps. Although the coarse position logic cannot function normally under these circumstances, during self-test operation the logic is forced to select specific (programmable) center taps in each of the Y and Z axes. The scatter in the fine positions derived from the preamplifier signal level outputs for a series of test pulses obtained with the same coarse position is a measure of the contribution of electronic noise to the position readout accuracy.

2.4. Operating conditions

The operating voltages applied across the MCPs (Table 1) are selected by exposing the imager to an x-ray source and slowly increasing the voltage in 25 V increments until the detected event rate stabilizes. The MCP voltages are then adjusted so that the ratio of valid to detected events is maximized. This corresponds to operation with a total MCP gain that exhibits the "cleanest" pulse height distribution with maximum discrimination between real events and low level electronic noise, and with minimal saturation of the pre-amplifiers or A/D converters for the largest pulse-height events. The system trigger level is set to trigger event detection for events with a pulse height just below the minimum in the pulse height distribution between the $1/f$ noise tail and the real event peak. The upper level discriminator setting is adjusted to veto only events that saturate the processing electronics (for such events the position determination algorithms do not work properly).

3. CALIBRATION RESULTS

Since the HSI is designed for the purpose of supporting the AXAF HRMA and HRMA/OTG calibrations, the imager subsystem level calibration plan was developed in accordance with the requirements of the HXDS error budget.[5] Although the imager's properties are characterized exhaustively by the subsystem level calibration plan, schedule constraints did not permit completion of these investigations prior to AXAF calibration. Furthermore, as previously noted, the MCP stack had to be replaced shortly before the AXAF calibration, thus invalidating any existing calibrations that depend on the individual properties of the MCPs.

Table 1. MCP High Voltage Settings

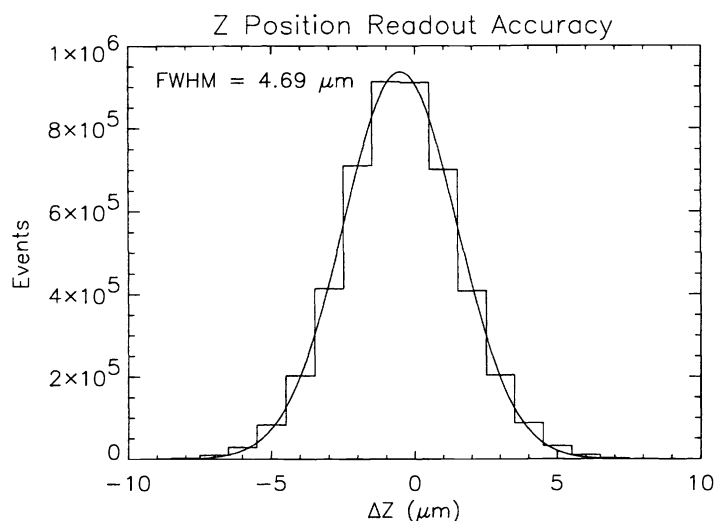| Electrode	Voltage
Ion Shield	$-2300\,\text{V}$
Permanent Mask	$-2500\,\text{V}$
MCP Top	$-2500\,\text{V}$
MCP Center	$-1375\,\text{V}$
MCP Bottom	$-300\,\text{V}$
Cross-grid	$+0\,\text{V}$
Reflector	$-150\,\text{V}$

Figure 3. Electronic noise contribution to the position readout accuracy, Z cross-grid.

In this section the calibration data that are available are discussed. The normal incidence quantum efficiency data were obtained after the MCP replacement and reflect the performance of the imager as used during AXAF calibration. All of the other calibration data were obtained with the earlier detector configuration. While these data do not reflect the exact performance of the imager as used during the AXAF calibration, they are included here as being representative of the detector's capabilities.

3.1. Position readout accuracy

The electronic noise contribution to the position readout accuracy of the imager is measured by running the detector in self-test mode. For this measurement the coarse position logic is programmed to select each of the cross-grid taps in sequence as the forced event center in Y and Z. For each center position, 315000 events are obtained. Once the digitized preamplifier signals are processed through the fine position algorithm, for each center tap selected by the coarse position logic, the mean position of all of the data obtained in that configuration is subtracted to determine deviations from the mean fine position. This step is necessary because the self-test signal coupling into the back MCP is not uniform; therefore the mean fine position will vary with the choice of center tap. Next, all of the data for each axis are combined, and the electronic contribution to the position readout accuracy is measured by fitting a Gaussian to the histogram of the fine position deviations. This is shown for the Z axis in Figure 3, where the Gaussian has a FWHM of $4.69\,\mu\text{m}$. The Y cross-grid data cannot be used to determine reliably the electronic noise contribution to the position readout accuracy since the Y cross-grid is partially shielded by the Z cross-grid.
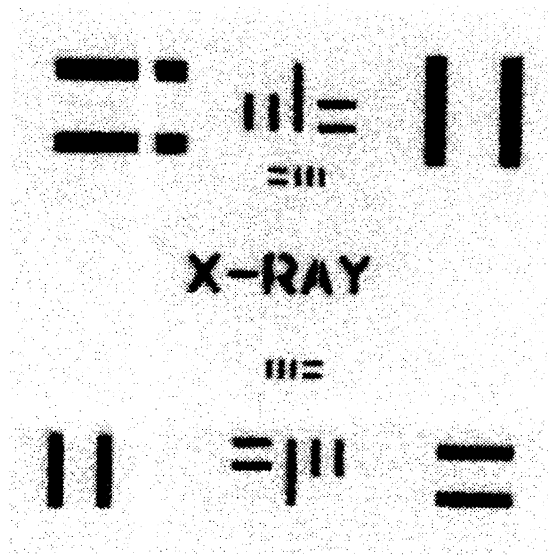
Figure 4. Spatial resolution mask image central region. The smallest slits are nominally $12.7\,\mu\mathrm{m} \times 76.2\,\mu\mathrm{m}$.

3.2. Spatial resolution

The spatial resolution of the imager is measured by replacing temporarily the ion shield and permanent mask assemblies with a resolution mask mounted in close proximity to the input surface of the front MCP. These data were obtained with the original MCP stack incorporating the CsI photocathode. The spatial resolution of the imager in the final configuration used for the AXAF calibrations has not been measured, but similar results to those reported here are anticipated. An image of the resolution mask, which comprises $\sim 12\,\mu\mathrm{m}$ thick electroformed Ni and incorporates a series of slits with known widths and separations, is obtained by exposing the detector to a source of C-Kα x-ray photons (Fig. 4). The integration time is selected so that ~ 1000 counts are obtained in each of the images of the smallest slits (nominally $12.7\,\mu\mathrm{m} \times 76.2\,\mu\mathrm{m}$). Since all of the slit pairs appear well resolved, the width of the line response function (LRF) is estimated by fitting profiles to the projections of the smallest slit images and subtracting in quadrature the nominal slit width. This method yields identical results in Y and Z, with a mean deconvolved LRF FWHM of $\sim 17.1 \pm 1.1\mu\mathrm{m}$ (Fig. 5).

3.3. Spatial linearity

The imaging distortion of the detector is measured in a similar manner to the spatial resolution, by replacing the ion shield and permanent mask assembly with a pinhole mask. Once again, these data were obtained with the original MCP stack incorporating the CsI photocathode and not the final system used for the AXAF calibrations. The mask is made of $\sim 51\,\mu\mathrm{m}$ thick electroformed Ni foil and incorporates a rectangular grid of $50\,\mu\mathrm{m}$ diameter pinholes on $500 \pm 2.0\,\mu\mathrm{m}$ centers. An image of the mask with ~ 1000 counts per pinhole is obtained using a C-Kα x-ray source. After applying the degap correction to the data, the centroid positions of the pinhole images are determined using a center-of-gravity algorithm. The measured pinhole image centroid positions are then compared to the expected positions for a perfectly uniformly spaced rectangular grid of pinholes. To minimize the root sum square difference between the observed and predicted pinhole positions, the Y and Z offsets, scale factor, and relative rotation between the data and the model are allowed to vary freely.

The residual position errors presented in Figure 6 map the local distortions in the imager. For clarity, the length of the error vectors have been scaled by a factor of 10 in the figure. A histogram of the magnitude of the position errors is shown in Figure 7, where a Gaussian plus a quadratic have arbitrarily been fitted to the data. The RMS deviation is $\sim 15.3\,\mu\mathrm{m}$, while the mode of the distribution is $\sim 9.3\,\mu\mathrm{m}$ and the peak error is $\sim 108\,\mu\mathrm{m}$. Clearly, the details of the distortion map depend in part on the degap correction applied to the data, and alternative degapping algorithms may result in larger or smaller distortion corrections. However, it seems unlikely that any
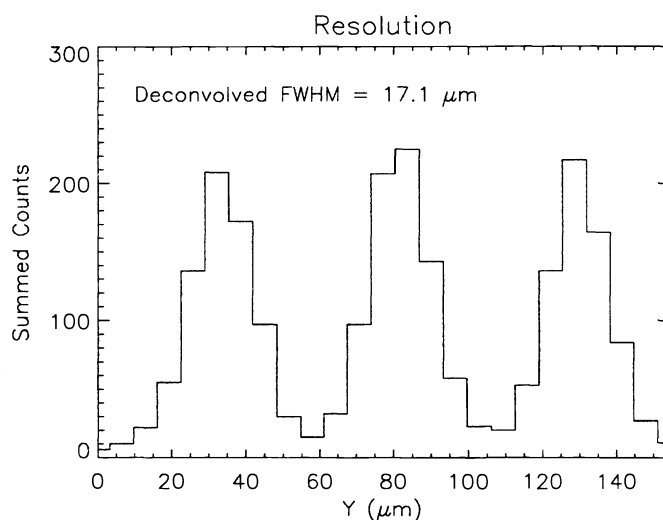
24

Figure 5. Measured line profiles for the smallest spatial resolution mask slit images.

simple degapping algorithm could eliminate the irregular distortions observed. Therefore some form of distortion correction applied after degapping appears to be essential for deriving accurate spatial information.

3.4. Quantum efficiency

Due to program schedule constraints, QE calibrations of the detector as used during the AXAF calibration have not yet been completed. The overall QE depends both on the incident x-ray energy and the angle between the incident rays and the axis of the front MCP pores.

For any given incident angle the QE is a smoothly varying function of energy, except near x-ray absorption edges. The absorption edges correspond to materials that comprise the glass used in the MCPs, the photocathode material (if applicable), and the materials used in the ion shield. For planning purposes during the AXAF calibration we used estimates for the QE from previous measurements of uncoated MCPs reported in the literature[3,4] multiplied by the predicted ion shield transmission estimated using the published Henke[6] x-ray absorption data. The average QE over the detector has been measured at a few energies for an incident x-ray beam normal to the MCP surface. These data are presented in Figure 8. Except for B-Kα, the statistical errors are of order a few percent, and the systematic errors are probably of similar magnitude. At the lowest energies the errors will be larger.

The angular dependence of QE has not yet been measured. Published data for uncoated MCPs[3,4] demonstrate that the QE can vary by factors of several depending on the incident photon angle. For low energy x-rays, rays parallel to the MCP pore axis see a low QE because most of the photons pass through the pores without impacting the side walls of the channels and causing an electron cascade. As the angle between the ray and the pore axis increases, the QE increases rapidly at first due to the increasing number of photons that impact the side walls of the channels, and then decreases as the geometric obscuration of the channel ends becomes larger and the fraction of x-rays that pass completely through the active layer of the glass responsible for the electron cascade increases. At higher energies photons impacting the interchannel "land" between the MCP pores may be a significant source of primary electrons even for zero incident angle. Many of these primary electrons will be captured by the ion shield and will not cause electron cascades.

Clearly, the variation of QE with incident angle depends in a complex and non-monotonic way on incident x-ray energy, implying that calibration of the anugular dependence at many energies is needed. Since the converging x-ray beam from the HRMA covers a range of incident angles (relative to the MCP pores which are tilted 6° to the normal to the imager) from ∼ 2° to ∼ 10°, deconvolution of the angular dependence of QE will be essential for successful analysis of any data obtained with the imager.
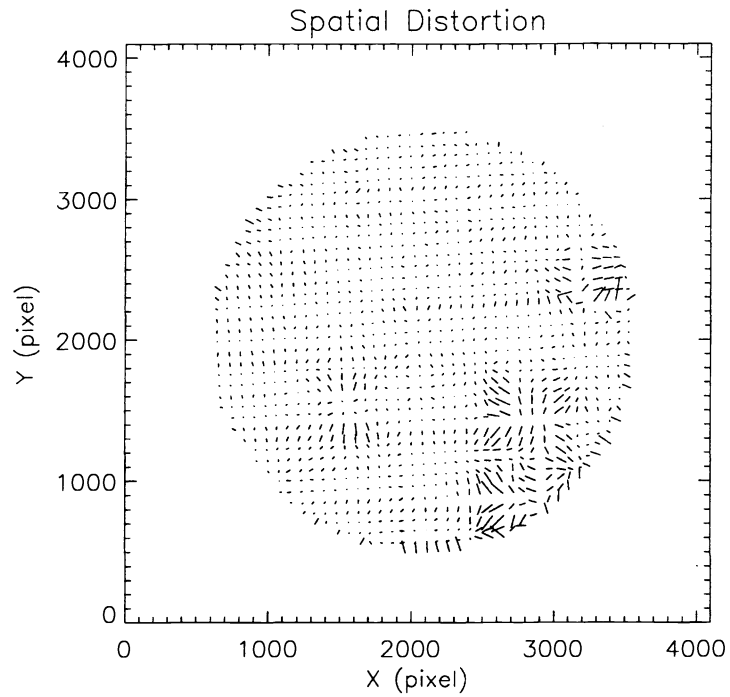
Figure 6. Residual distortion map. The length of the error vectors have been scaled by a factor of 10.
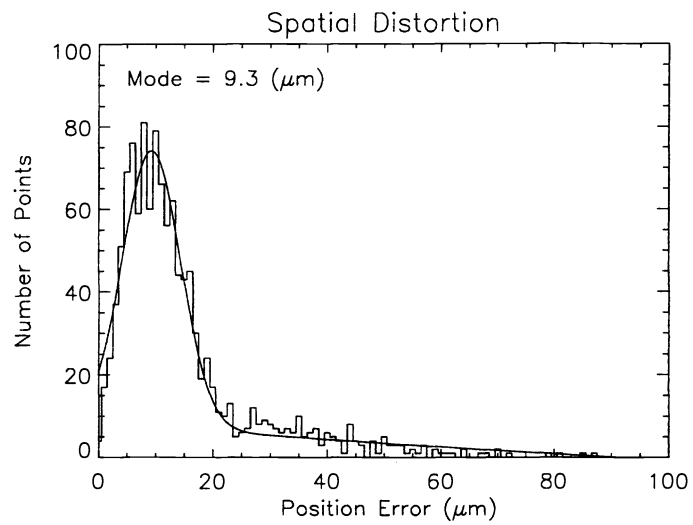

Figure 7. Histogram of position errors derived from the data in Figure 6.
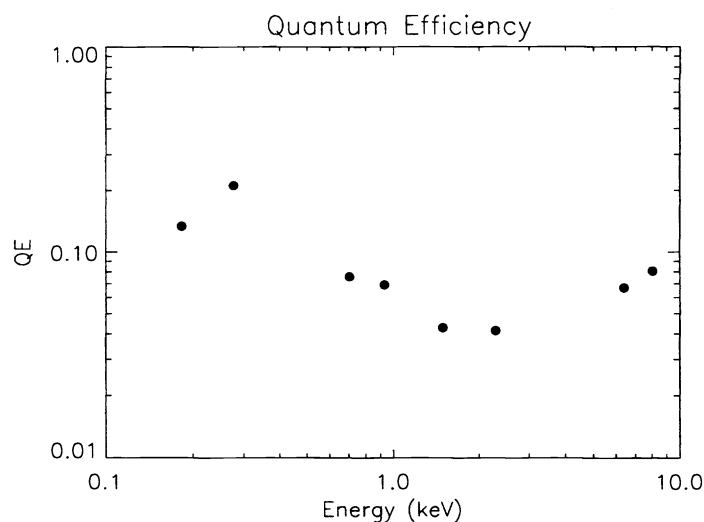
26

Quantum Efficiency

Figure 8. Measured QE for normal incidence.

Limited flat field data have been obtained. Summing over all energies for which data are available yields a statistical accuracy of about 3% for 1 mm × 1 mm ($\sim 20'' \times 20''$) areas. Where flat field data are available for individual energies, the statistical accuracies for 1 mm × 1 mm areas varies between $\sim$5% and $\sim$20%, depending on energy. Flat field information is not available on arcsecond scales.

3.5. Counting rate linearity

The linearity of observed counting rate with incident x-ray flux for the imager has not yet been measured in detail. Verification tests performed with the imager using the CsI coated MCP stack indicate that the count rate linearity of the post-processing electronics is no worse than $\sim$2% for count rates between $\sim$100 Hz and $\sim$2000 Hz. For rates above $\sim$2100 Hz the counting electronics saturate rapidly, so that the maximum reported rate is of order 2300 Hz irrespective of incident flux level. The measured maximum counting rate is in excellent agreement with the theoretical value determined from a queuing theory analysis of the counting electronics FIFO buffer.

A detailed investigation of gain depression and pore saturation effects that occur at high per-pore count rates has yet to be conducted. Preliminary data suggest that the response of individual pores is degraded by a few percent for a per-pore count rate $\sim$10 Hz. For the AXAF PRF, this corresponds to a total point source count rate of order 100 Hz, which is a level used extensively during the AXAF HRMA calibration. Further calibration of the imager is required to quantify these effects accurately.

4. HSI AXAF CALIBRATIONS

Phase 1 of the AXAF HRMA and OTG calibration is designed to characterize the x-ray optic and gratings with sufficient precision that accurate models of the on-orbit performance can be developed from the calibration data. During this phase the HXDS is used to obtain x-ray data, and the HSI is the only imaging detector that is incorporated into the HXDS. After phase 1, the HXDS (including the HSI) is removed and calibrations of the combined HRMA and flight instruments are conducted.

Although both the HRC and the AXAF CCD Imaging Spectrometer (ACIS) flight instruments are imaging detectors, for calibration purposes the HSI still offers some unique capabilities. Specifically, the imaging resolution of the HSI is better than ACIS ($\sim$17 μm for the HSI versus $\sim$48 μm two-pixel resolution for ACIS), and the count rate capability of the HSI is a factor of 10 better than the HRC — essential for gathering high S/N data when constrained by a limited time schedule.
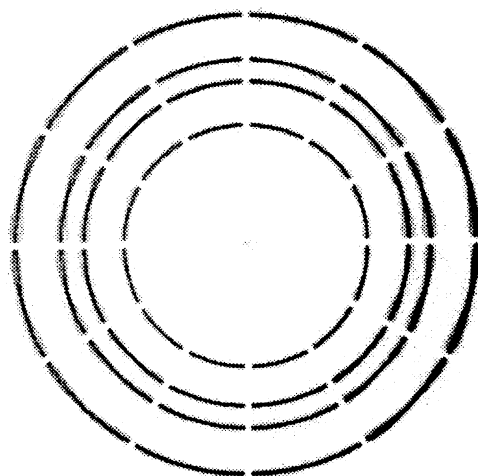
27

Figure 9. Example AXAF HRMA ring focus image. The HSI image has been degapped. Note the increase in apparent ring intensity from left to right, caused by the angular dependence of QE.
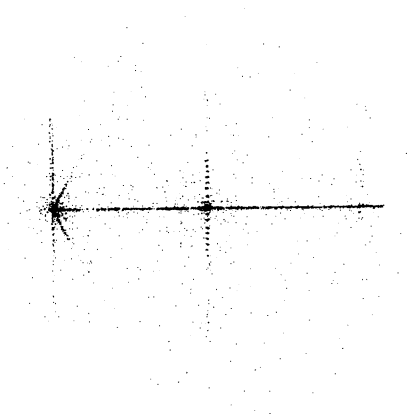

Figure 10. Example AXAF HRMA/OTG low energy grating image. The zeroth order is just visible partly occulted by the permanent mask on the left side of the image, the first order is in the center of the image, and the second order is visible faintly to the right of the image.

During phase 1, the HSI is used extensively to (a) support focus measurements of the HRMA and OTGs (including HRMA first light), (b) image the "outer core" ($\sim 1''-10''$ radius) of the HRMA PRF while using the permanent mask cusps to obscure the bright inner core of the PRF, (c) obtain images at the HRMA ring focus, and (d) image the dispersed orders from the OTGs providing data on spectral resolution, line profiles, and effective areas. Many of these calibrations could not be performed without an imaging detector with the resolution and count rate capabilities of the HSI. Although it is beyond the scope of this paper to describe the results of the the AXAF calibrations, sample HSI images are provided in Figures 9–10 to demonstrate the typical quality of the imager data.

28

ACKNOWLEDGEMENTS

REFERENCES

1. S. E. Pearce, J. E. Lees, J. F. Pearson, G. W. Fraser, A. N. Brunton, K. A. Flanagan, A. T. Kenter, M. Barbera, V. Dhanak, A. Robinson, and D. Teehan, "Synchrotron calibration of alkali halide coated microchannel plate detectors in the 50–350 and 2000–6000 ev bands," in *EUV, X-Ray, and Gamma-Ray Instrumentation for Astronomy VI*, O. H. W. Siegmund and J. V. Vallerga, eds., *Proc. SPIE* **2518**, pp. 322–335, 1995.

2. A. T. Kenter, K. A. Flanagan, G. R. Meehan, S. S. Murray, and M. V. Zombeck, "Microchannel plate testing and evaluation for the axaf high resolution camera (hrc)," in *EUV, X-Ray, and Gamma-Ray Instrumentation for Astronomy VI*, O. H. W. Siegmund and J. V. Vallerga, eds., *Proc. SPIE* **2518**, pp. 356–374, 1995.

3. G. W. Fraser, *X-ray Detectors in Astronomy*, Cambridge University Press, Cambridge, 1989.

4. E. Kellogg, P. Henry, S. Murray, and L. V. Speybroeck, "High-resolution imaging x-ray detector," *Rev. Sci. Instrum.* **47**, pp. 282–290, 1978.

5. E. M. Kellogg, *HXDS Error Budget & Performance Prediction*, Smithsonian Astrophysical Observatory, Cambridge, 1996.

6. B. L. Henke, P. Lee, T. J. Tanaka, R. L. Shimabukuro, and B. K. Fujikawa, "Low-energy x-ray interaction coefficients: photoabsorption, scattering and reflection," *At. Data Nucl. Data Tables* **27**, p. 1, 1982.